



# Quantifying and Comparing the Near-Field Enhancement, Photothermal Conversion, and Local Heating Performance of Plasmonic SiO<sub>2</sub>@Au Core-Shell Nanoparticles

Meijie Chen<sup>1,2</sup> · Yurong He<sup>1,2</sup>  · Jiaqi Zhu<sup>3</sup>

Received: 10 September 2018 / Accepted: 16 November 2018  
© Springer Science+Business Media, LLC, part of Springer Nature 2018

## Abstract

In this work, the finite element method and two-temperature model were used to optimize the near electric field, photothermal conversion efficiency, and local heating of SiO<sub>2</sub>@Au core-shell nanoparticles (NPs) using water as the dispersion medium. The optimal core-shell sizes to achieve maximum near electric field enhancement, photothermal conversion efficiency, and local heating were 14 nm/6 nm, 8 nm/3 nm, and 24 nm/12 nm. The optimized core-shell ratio decreased with increasing the optimized wavelength for both near electric field and photothermal conversion optimizations. In the local heating or temperature increase, due to the existence of thermal boundary conductance, a temperature drop was observed between the electrons and the lattice, the electrons and the dielectrics, and the NP and the surrounding water. All these barriers and high absorption ability led to a temperature increase in the NP region. All optimized core-shell NPs achieved surface plasmon resonance for different targets. Comparison between different optimized targets with a normalized processing function indicated a smaller optimized core-shell size and core-shell ratio were obtained with a consideration of greater effect of the NP radius.

**Keywords** Near field · Local heating · Plasmonic nanoparticle · Photothermal conversion

## Introduction

Plasmonics has become one of the most attractive fields of modern research due to interest in manipulating the interactions between metals and electromagnetic (EM) waves in a field for many applications [1, 2]. Plasmonics allows EM waves to be localized, guided, and manipulated beyond the diffraction limit and down to the nanoscale. One of the key components of plasmonic structures is the metal, whose free electrons can couple with incident EM, leading to a collective oscillation between these electrons and the incident light. These surface plasmon polariton modes are known as

localized surface plasmon resonance (LSPR) and propagating surface plasmon resonance (PSPR) when spatially confined in a metal nanostructure [3, 4].

The use of metal nanoparticles (NPs) in surface plasmon resonance (SPR) can enhance the near electric field on the nanoscale and light absorption, leading to pronounced heat generation and temperature increase in the NPs. The enhanced near electric field of plasmonic nanostructures can be used to enhance the efficiency of solar cells [5], as the near electric field enhancement associated with surface plasmon excitation can enhance charge carrier generation [6]. For example, the effect of near electric field enhancement around plasmonic NPs was reported to increase the photocurrents in dye-sensitized solar cells [7] and polymer-based organic solar cells [8]. Another approach to implement metal particles in solar cell systems is to take advantage of the high absorption or scattering cross section of the metal particles at the SPR wavelengths to redirect light into the solar cell. For instance, a photocurrent was generated by the SPR excitation of Au or Ag NPs adsorbed onto TiO<sub>2</sub> in such a solid-state plasmonic solar cell [9]. Plasmonic Au or Ag NPs have also been applied to enhance the solar absorption performance of direct solar absorption collectors [10–13]. Finally, the plasmon energy is partially converted to Joule heat by thermal resistance loss,

---

✉ Yurong He  
rong@hit.edu.cn

<sup>1</sup> School of Energy Science & Engineering, Harbin Institute of Technology, Harbin 150001, China

<sup>2</sup> Heilongjiang Key Laboratory of New Energy Storage Materials and Processes, School of Energy Science & Engineering, Harbin Institute of Technology, Harbin 150001, China

<sup>3</sup> Center for Composite Materials, Harbin Institute of Technology, Harbin 150001, China

resulting in a strongly localized temperature increase when the field is strongly localized. This effect constitutes the basis of the emerging field of thermoplasmonics, which can be used in the biomedicine field as “light-activated nanoscopic heaters.” Au and SiO<sub>2</sub>-coated Au NPs have been tested for use as a plasmonic photothermal therapy [14, 15] in which cancer cells are selectively labeled with the plasmonic NPs and then irradiated with a light source, resulting in selective heating and destruction of the cancer cells without destroying healthy cells.

The approach of using noble metal plasmonic core-shell NPs for selective targeting is general and versatile. A great deal of work has been devoted to investigating the ability of plasmons to enhance various processes of interest and improve sensing and light management applications. In all of these applications, optimal design of the plasmonic structures is crucial to producing the desired field enhancement at the designated spatial locations. The near electric field, light absorption, and heat generation of metal NPs depend on their composition, morphology, environment, and illumination wavelength. A particularly interesting class of plasmonic structures is the metallic shells with dielectric cores. For the metal part, plasmon Au metal has the strong surface plasmon resonance factor at the visible and near-infrared region, which is also stable with good biocompatibility [16]. On the other hand, development of dielectric nanoparticles with improved properties has been studied in several areas such as synthesis and surface science [17]. SiO<sub>2</sub> particles still occupy a prominent position in scientific research, because of their easy preparation and their wide uses in various industrial applications, such as catalysis, pigments, pharmacy, electronic and thin film substrates, electronic and thermal insulators, and humidity sensors [18]. Therefore, in this work, we combine the finite element method (FEM) and the two-temperature model (TTM) to optimize the near electric field enhancement, photothermal conversion, and temperature increase of SiO<sub>2</sub>@Au NPs using water as a dispersion medium. Different optimum dimensions were obtained depending upon whether enhancement of the near electric field and photothermal and temperature increase was targeted.

## Methods

### Optical Simulations

In this work, the FEM was used to evaluate the optical properties of the plasmonic core-shell NPs, which are illustrated schematically in Fig. 1a. EM propagation in this system can be described as follows [19]:

$$\nabla \times (\mu_r^{-1} \nabla \times E) - k_0^2 \left( \varepsilon_r - j \frac{\sigma}{\omega \varepsilon_0} \right) E = 0 \quad (1)$$

$$Q_r = \frac{1}{2} \operatorname{Re} \left( \int J \cdot E \right) \quad (2)$$

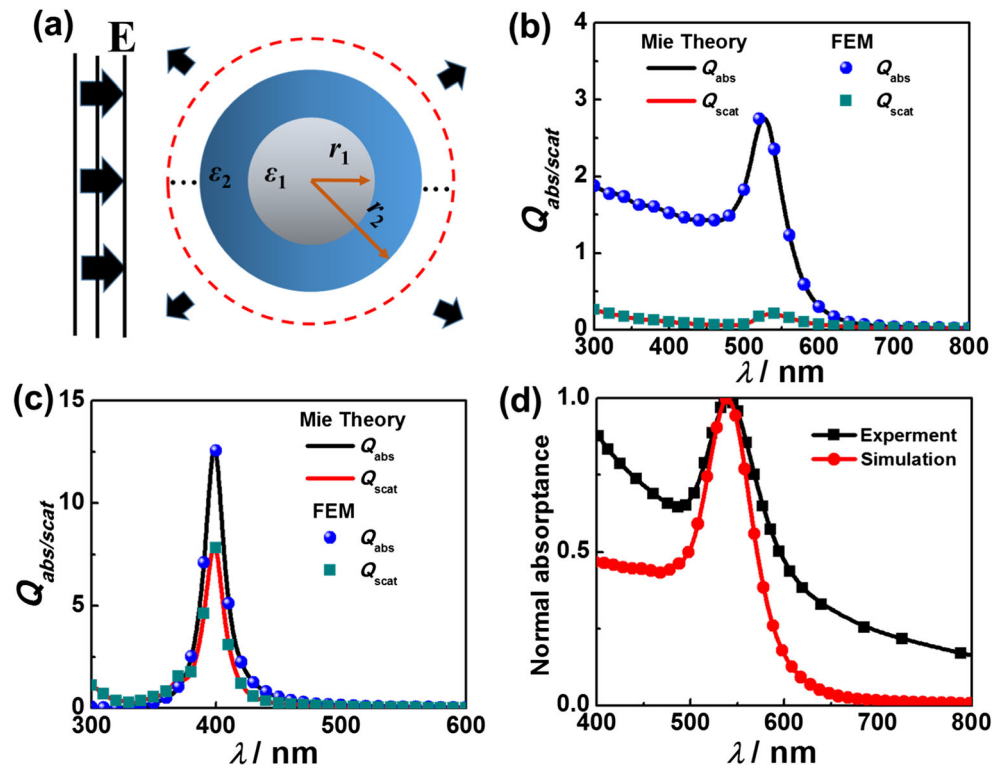
where  $E$  is the electric field of the medium,  $J$  is the current density,  $Q_r$  is the thermal resistance loss,  $k_0$  is the wavenumber,  $\varepsilon_r$  is the dielectric function, which is calculated as  $\varepsilon_r = (n - ik)^2$ , and  $n$  and  $k$  are the complex refractive index. These equations can be solved using the commercial software package COMSOL Multiphysics. First, the basic properties of each domain are defined. Secondly, the external and internal boundary conditions, including the perfect absorption boundary, continuous boundary, and periodic boundary conditions, are set strictly. Then, the properties of the EM waves in the domain are set, including the incident EM wave type, incident direction, and intensity. Finally, the solve domains are meshed, and the EM field distribution can be obtained by solving the EM propagation equations based on the FEM.

To verify this model, a comparison between the simulated results from the FEM and Mie theory was carried out for Au NPs (radius = 20 nm) embedded in water, and the results are shown in Fig. 1b. The absorption and scattering cross sections calculated using the FEM were in good agreement with the Mie theory results. In addition, another Ag NP with a radius of 20 nm was also verified between the Mie theory and FEM in Fig. 1c; a good agreement was also obtained, indicating that accurate results can be obtained using the FEM. Finally, a comparison of the experimental results from ref. [20] and simulation results for the SiO<sub>2</sub>@Au core-shell NP (diameter of Au core is 50 nm and the thickness of the SiO<sub>2</sub> shell is 80 nm) was conducted in Fig. 1d. It can be seen that the peak wavelengths agree well at ~540 nm. And the experimental absorptance was broader than that of the simulation results, which can be attributed that the NP size in the experiments was not so consistent, and it may contain some other NP sizes.

### Heat Transfer Simulation

As shown in Fig. 2, when light is irradiated on a NP surface, different physical heating processes occur at different time scales [21]. Within the first ~100 fs, the interaction between the photon and the electron is dominant, leading to a great temperature increase in the electron. Subsequently, electron-lattice relaxation occurs at 100 fs to 10 ps, in which the heat is transferred from the electron to the lattice. Finally, the heat is dissipated into the surrounding media from the lattice after 100 ps. When the irradiation in the photothermal process is provided by a femtosecond or picosecond pulsed laser, the different physical processes originating from the electrons and the lattice should be analyzed and taken into account. The TTM is only valid for thermal analysis of the

**Fig. 1** Computational model of the plasmonic core-shell NP (a). Comparison of the simulated results obtained using the FEM and Mie theory for Au (b) and Ag (c) NPs (radius = 20 nm) embedded in water. Comparison of the experimental results and simulation results for the SiO<sub>2</sub>@Au core-shell NP (diameter of Au core is 50 nm and the thickness of the SiO<sub>2</sub> shell is 80 nm) (d)



photothermal process, in which the electrons and the lattice are defined as two distinct temperature regions and solved by coupling several heat transfer steps. Steady-state CW light illumination is considered using heat transfer simulation. The electron and lattice temperatures are defined as  $T_e$  and  $T_l$ , respectively, in the TTM. These temperatures are assumed to be uniform throughout each layer due to their large thermal conductivity and small size compared with the water medium. Therefore, the temperatures are the only unknowns in the heat transfer equations.

**Heat Transfer for a Single Layer NP** First, the steady-state heat transfer of a single layer NP in water was investigated, as shown in Fig. 2a. At the steady state, the absorbed

power is transferred from the light to the electrons, then to the lattice, and finally to the water medium. The electron-lattice coupling process can be described as follows [22, 23]:

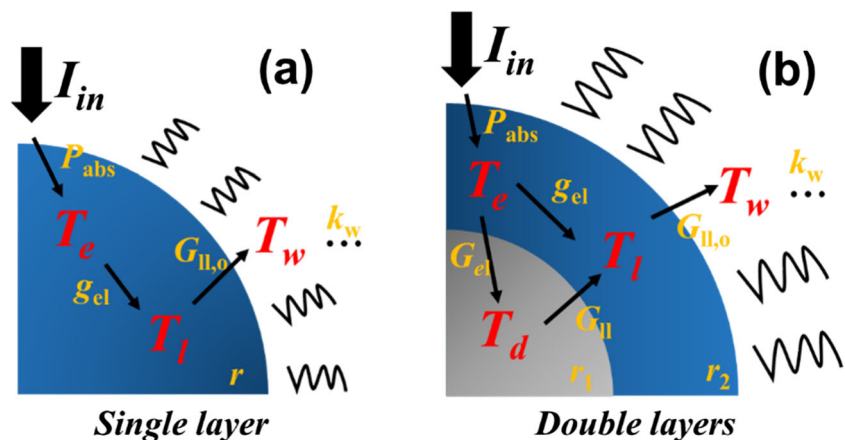
$$P_{\text{abs}} = g_{\text{el}}(T_e - T_l)V \quad (3)$$

$$P_{\text{abs}} = I_{\text{in}}\sigma_{\text{abs}} \quad (4)$$

$$V = \frac{4}{3}\pi r^3 \quad (5)$$

where  $P_{\text{abs}}$  is the absorbed power,  $g_{\text{el}}$  is the electron-lattice coupling coefficient ( $3 \times 10^{16} \text{ W} \cdot \text{m}^{-3} \cdot \text{K}^{-1}$  for gold [24]),  $V$  is the NP volume,  $I_{\text{in}}$  is the incident light intensity,  $\sigma_{\text{abs}}$  is the absorption cross section, and  $r$  is the NP radius.

**Fig. 2** Thermal response of single layer (a) and double layer (b) NPs, labeled with the parameters used in the modeling of heat transfer processes



The heat transfer between the NP and water can then be described by considering thermal boundary conductance (TBC):

$$P_{\text{abs}} = G_{\text{lw}}(T_l - T_w)S \quad (6)$$

$$S = 4\pi r^2 \quad (7)$$

where  $G_{\text{lw}}$  is the TBC ( $105 \text{ MW} \cdot \text{m}^{-2} \cdot \text{K}^{-1}$  for gold [25]),  $S$  is the NP surface area, and  $T_w$  is the temperature of the water.

Finally, heat dissipation in the water can be described as follows:

$$P_{\text{abs}} = 4\pi Rk_w(T_w - T_0) \quad (8)$$

where  $k_w$  is the thermal conductivity of the media ( $0.6 \text{ W} \cdot \text{m}^{-1} \cdot \text{K}^{-1}$  for water),  $R$  is the distance from the center, and  $T_0$  is the temperature of the surrounding environment.

**Heat Transfer for Double Layers** As discussed above, a series of nonlinear equations can be written for the thermal responses of the double layer structure shown in Fig. 2b. First, light is absorbed by the electrons in the metallic layer [26]:

$$P_{\text{abs}} = g_{\text{el}}(T_e - T_l)V_1 + G_{\text{el}}(T_e - T_d)S_1 \quad (9)$$

$$V_1 = \frac{4}{3}\pi(r_2 - r_1)^3 \quad (10)$$

$$S_1 = 4\pi r_1^2 \quad (11)$$

where  $V_1$  is the metallic layer volume,  $G_{\text{el}}$  is the electron-lattice conductance of the interface between the metal and dielectric ( $(96 + 0.189T_e)\text{MW} \cdot \text{m}^{-2} \cdot \text{K}^{-1}$  for the interface between Au and  $\text{SiO}_2$  [27]),  $r_1$  and  $r_2$  are the radii of the dielectric and metal layers, respectively,  $T_d$  is the temperature of the dielectric layer, and  $S_1$  is the surface area of the dielectric layer.

Then, the heat transfer among the lattice, the dielectric layer, and the water can be described by considering the TBCs:

$$g_{\text{el}}(T_e - T_l)V_1 = G_{\text{ll}}(T_l - T_d)S_1 + G_{\text{lw}}(T_l - T_w)S_2 \quad (12)$$

$$S_2 = 4\pi r_2^2 \quad (13)$$

where  $G_{\text{ll}}$  is the lattice-lattice conductance of the interface between the metal and the dielectric ( $141.5 \text{ MW} \cdot \text{m}^{-2} \cdot \text{K}^{-1}$  for the interface between Au and  $\text{SiO}_2$  [27]) and  $S_2$  is the outer surface area of the metal layer.

A similar energy balance can also be applied to the dielectric layer and can be described as follows:

$$G_{\text{ll}}(T_l - T_d)S_1 + G_{\text{el}}(T_e - T_d)S_2 = 0 \quad (14)$$

Finally, the heat is dissipated in the water, which can be described using Eq. 8. These nonlinear equations can be solved using MATLAB programs.

## Parameter Optimization Models

In this study, several optimization targets were studied for different photothermal conversion applications.

**Model for the Optimization of the Enhancement of the Near Electric Field** For optimization of the near electric field, a dimensionless parameter  $\varepsilon$  that quantifies the ability of the NP to enhance the near electric field intensity in the surrounding media is defined as follows:

$$\varepsilon = \left| \frac{E_{\text{max}}}{E_{\text{in}}} \right|^2 \quad (15)$$

where  $E_{\text{in}}$  is the intensity of the external electric field and  $E_{\text{max}}$  is the maximum intensity of the electric field in the surrounding media.

**Model for Optimization of Photothermal Conversion** For effective photothermal conversion, the light absorption of the NP must be maximized. Lalis et al. [28] developed a dimensionless parameter to quantify the photothermal conversion efficiency of a NP, which can be expressed as follows:

$$\eta = \frac{\lambda_{\text{ref}}\sigma_{\text{abs}}}{2\pi V} \quad (16)$$

where  $\lambda_{\text{ref}} \approx 1240 \text{ nm}$  is the reference wavelength.  $\sigma_{\text{abs}}$  is the absorption cross section of the NP.  $V$  is the NP volume.

**Model for the Optimization of Local Heating** For applications requiring the enhancement of local heating, the ability to achieve a high temperature within the NP is targeted. Therefore, the temperature increase  $\Delta T$  at the interface between the NP and water was optimized, which can be obtained as described in the “Heat Transfer Simulation” section.

## Results and Discussion

Fig. 3 illustrates the enhanced near field, photothermal conversion, and local heating conditions in a plasmonic core-shell composed of an Au layer with a  $\text{SiO}_2$  shell immersed in water under ambient conditions. The NP parameters are optimized to provide enhanced near field, photothermal conversion, and local heating performance for different applications. When light is irradiated onto the NP surface, the NP surface generates an enhancement of the near electric field, which enhances the light absorption of the NP. The absorbed light power is then transferred via different heat transfer channels: coupling between the electrons and the lattice modes inside the metal layer (mediated by the volumetric transfer coefficient  $g_{\text{el}}$ ) and coupling between these degrees of freedom and the lattice



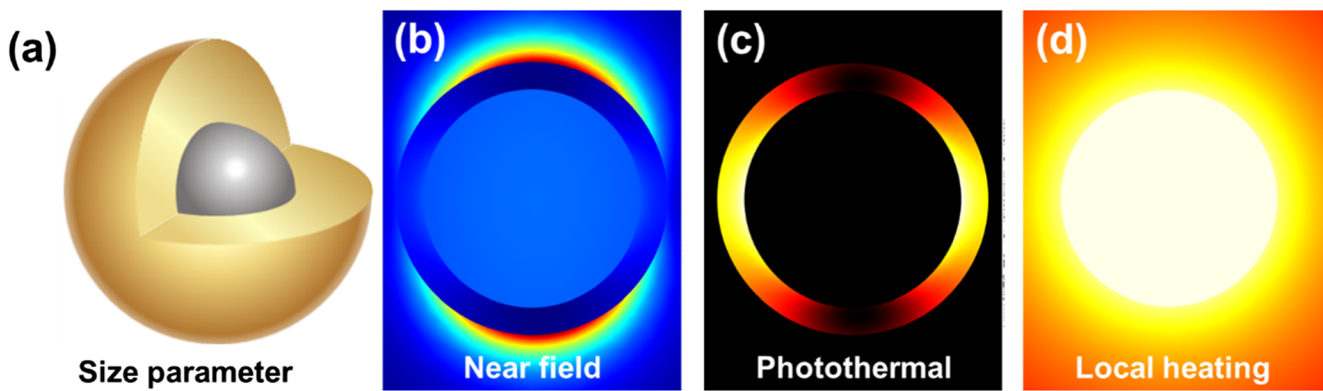


**Fig. 3** Schematic of near electric field enhancement, photothermal conversion, and local heating in a plasmonic core-shell. Schematic view of a plasmonic core-shell NP with metallic and dielectric layers (a).

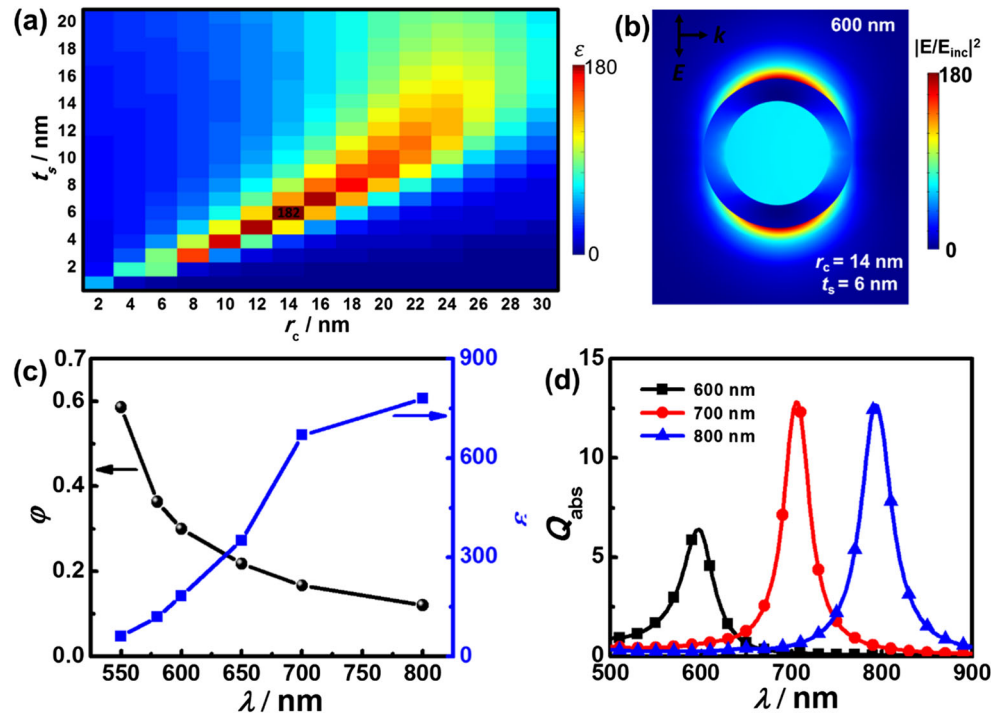
Illustration of the optimized near electric field enhancement (b), photothermal conversion (c), and temperature increase (d) in a Au shell with a SiO<sub>2</sub> core

modes in the surrounding dielectrics with TBCs of  $G_{el}$  and  $G_{ll}$  (see “Heat Transfer Simulation” section). Finally, the heat dissipates into the water in the surrounding environment through the metal-water interface with a TBC of  $G_{ll, o}$ . In this work, the enhancement of the near electric field ( $\varepsilon$ ), photothermal conversion ( $\eta$ ), and local heating ( $\Delta T$ ) performance have been optimized individually. To optimize these parameters, SiO<sub>2</sub>@Au core-shell NPs with core radii ranging from 2 to 30 nm with an interval of 2 nm and shell thicknesses of 1 nm to 20 nm with an interval of 1 nm have been investigated at different wavelengths with a consideration of the NP preparation process and more sensitive of the shell thickness.

### Optimization of the Enhancement of the Near Field

Figure 4a shows the optimization results of the NP size to maximize near electric field intensity at a wavelength of 600 nm for SiO<sub>2</sub>@Au core-shell NPs. Among all the simulated dimensions, the optimized SiO<sub>2</sub>@Au NP core-shell size dimension was 14 nm ( $r_c$ )/6 nm ( $t_s$ ), with maximum enhanced near electric field factors ( $\varepsilon$ ) of 182, as shown in Fig. 4b. In addition, the optimized core-shell ratios, defined as  $\varphi = t_s/(r_c + t_s)$ , was 0.3, which was nearly identical along with maximum near electric field enhancements in each row as shown in Fig. 4a. It indicated that the LSPR wavelengths were located at 600 nm with the core-shell ratio of  $\sim 0.3$ .

**Fig. 4** Optimization of the NP dimensions to maximize near electric field intensity at a wavelength of 600 nm for SiO<sub>2</sub>@Au core-shell NPs. **a** Contour plot of the maximum near electric field intensity enhancement. **b** Contour plots of the near electric field intensity for SiO<sub>2</sub>@Au NPs with core-shell dimensions of 14 nm/6 nm. **c** Optimized core-shell ratio and maximum near field at different wavelengths. **d** Absorption efficiencies at the optimized results for different optimized wavelengths



However, an optimized size parameter ( $r_c = 14$  nm and  $t_s = 6$  nm) can be obtained that occurs LSPRs at 600 nm. To further understand the dependence of the core-shell ratio on the irradiation wavelength, different optimized wavelengths were considered, and the results of the optimized core-shell ratio and maximum near field are shown in Fig. 4c. It can be seen that the optimized core-shell ratio decreased with increasing the optimized wavelength, as a thinner plasmonic shell results in a longer LSPR wavelength. And the maximum intensity of near field increased rapidly and then changed slightly with increasing the optimized wavelengths since a gradually smaller core-shell ratio limited the LSPR intensity. Figure 4d shows the absorption efficiencies at the optimized results for different optimized wavelengths. The optimal core-shell dimensions were 20 nm/4 nm and 22 nm/3 nm at wavelengths of 700 nm and 800 nm, respectively. The optimized results agreed well with the LSPR wavelengths, indicating the enhanced near field contributed to the enhanced absorption ability. And the peak absorption efficiency also increased rapidly at the short optimized wavelengths and then changed little at the long optimized wavelength. These results were in good agreement with our previous work about the optimized absorption efficiencies [29].

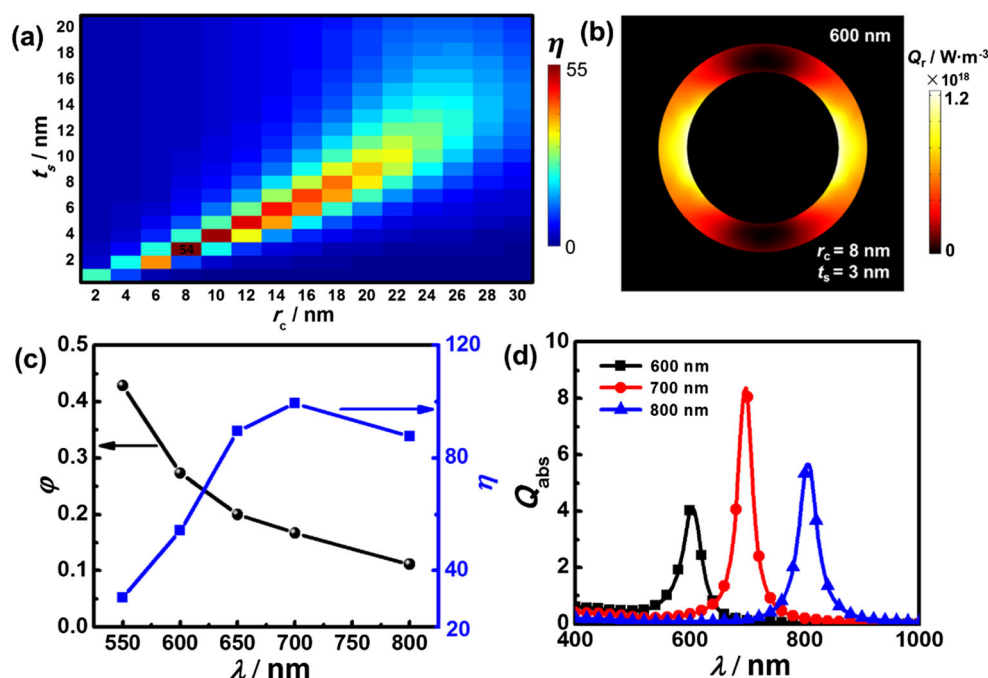
## Optimization of Photothermal Conversion

Figure 5a shows the optimization of the NP dimensions to maximize photothermal conversion at a wavelength of 600 nm. Among all the simulated dimensions, the SiO<sub>2</sub>@Au NP core-shell dimensions were 8 nm/3 nm with an optimized photothermal conversion factor of 54, which is much higher

than that of the single component plasmonic NPs [28]. The contour plot obtained for the maximization of the near electric field enhancement are similar to those for photothermal conversion, as shown in Figs. 4a and 5a. Figure 5b shows the optimized NPs showed similar thermal resistance loss distributions. An enhanced thermal resistance loss can be obtained in the inner cavity of the Au shell due to the cavity resonance mode. The same calculations were carried out for different targeted wavelengths, and the results are shown in Fig. 5c. Similarly, the core-shell ratio decreased with increasing the optimized wavelengths. And the photothermal conversion factor increased rapidly and then decreased with increasing the optimized wavelengths. Figure 5d shows the absorption efficiencies at the optimized results for different optimized wavelengths. The optimal core-shell dimensions were 10 nm/2 nm and 8 nm/1 nm at wavelengths of 700 nm and 800 nm, respectively. The optimized results agreed well with the LSPR wavelengths. And the peak absorption efficiency also increased rapidly at the shorter optimized wavelengths and then decreased at the longer optimized wavelength.

However, it must be emphasized that most works use the absorption efficiency (i.e., absorption across section normalized by the cross-sectional area) to characterize the photothermal conversion ability of NPs, and thus the results obtained from this method should be treated with caution. Figure 6 shows the optimization of the absorption cross section and absorption efficiency normalized by the cross section at a wavelength of 600 nm. It can be seen that the absorption cross section increased with increasing the NP size and then reach the maximum absorption cross section ( $2.76 \times 10^{-14}$  m<sup>2</sup>) with the optimal core-shell dimensions of 26 nm/14 nm as

**Fig. 5** Optimization of the photothermal conversion in the plasmonic SiO<sub>2</sub>@Au core-shell NPs at a wavelength of 600 nm. **a** Contour plot of the photothermal conversion performance. **b** Contour plots of thermal resistance loss for SiO<sub>2</sub>@Au core-shell NPs with core-shell dimensions of 8 nm/3 nm. **c** Optimized core-shell ratio and photothermal conversion factor at different wavelengths. **d** Absorption efficiencies at the optimized results for different optimized wavelengths



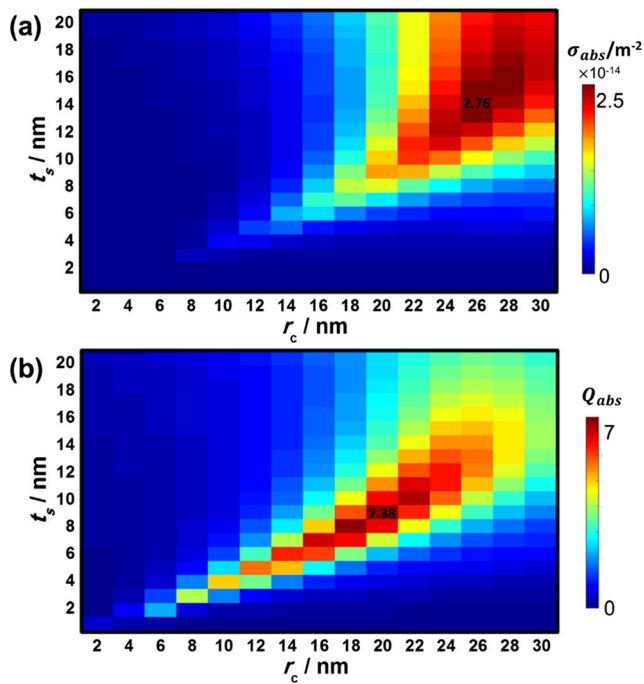


**Fig. 6** Optimization of the absorption cross section (a) and absorption efficiency normalized by the cross section (b) at a wavelength of 600 nm for SiO<sub>2</sub>@Au core-shell NPs

shown in Fig. 6a. Finally, the absorption cross section did not increase any more with an increase NP size due to the enhanced scattering effect. When the absorption cross section normalized by the cross-sectional area (i.e., absorption

efficiency) was considered, the optimal core-shell dimensions were 20 nm/9 nm in Fig. 6b. The reason for the discrepancy between the results of the absorption efficiency and photothermal conversion factor can be attributed to the fact that absorption efficiency does not consider the whole volume of the NP and is only a dimensionless parameter. However, the absorption cross section normalized by the NP volume takes into account the effect of the size of the NP on its photothermal conversion performance. Therefore, the photothermal conversion factor is a more accurate parameter for the calculation or evaluation of the photothermal conversion ability of the NPs.

### Optimization of Local Heating

Finally, the optimization of local heating, i.e., the increase in nanoparticle temperature, was calculated as described in the “Heat Transfer Simulation” section. Figure 7 shows the optimization of the local heating parameters for the SiO<sub>2</sub>@Au core-shell structures at a wavelength of 600 nm. The optimized dimensions for this target were very different from those obtained in the optimization of the near electric field enhancement and photothermal conversion due to the heat dissipation related to the NP surface and volume. As shown in Fig. 7a, the optimal core-shell dimensions to maximize local heating were 24 nm/12 nm. And its LSPR wavelength was located in the wavelength of 600 nm as shown in Fig. 7c. Figure 7d, e show near electric field intensity enhancement

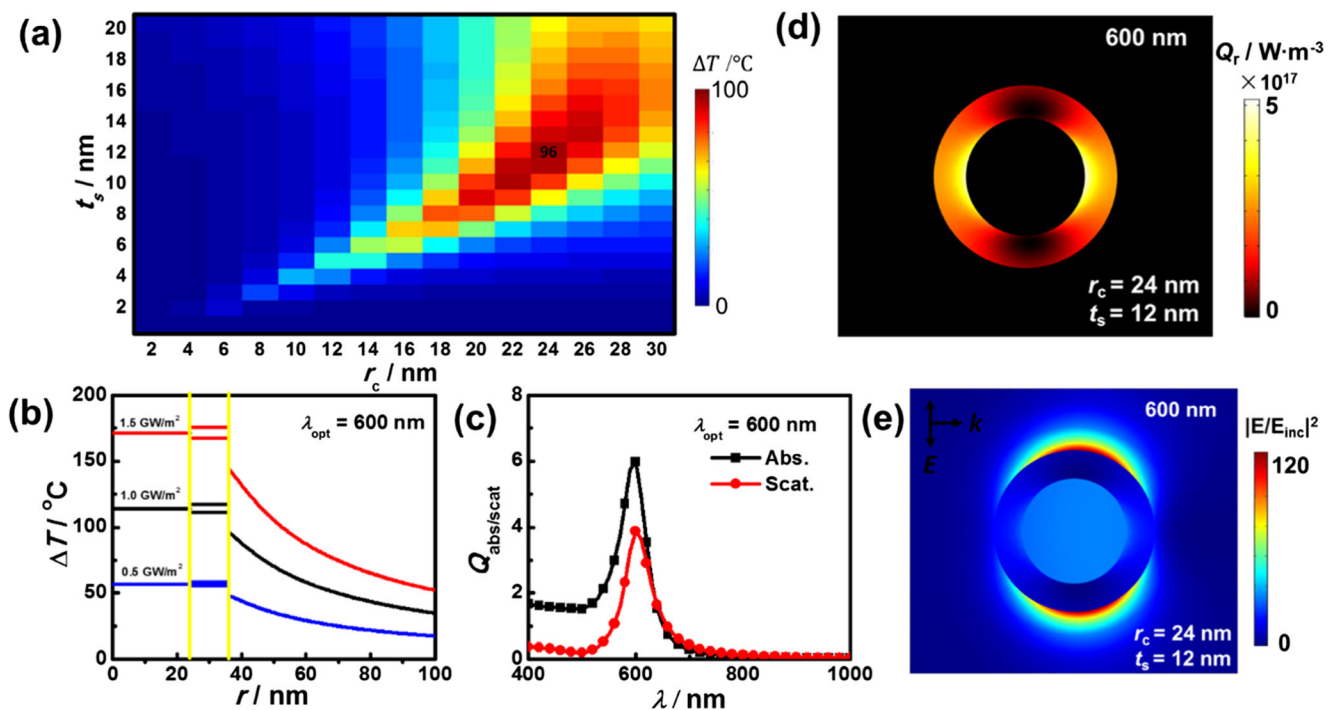


**Fig. 7** Optimization of the temperature increase in SiO<sub>2</sub>@Au core-shell NPs at a wavelength of 600 nm. **a** Contour plots of the temperature increase for various core-shell sizes. **b–e** Temperature increase,

absorption efficiency, near electric field intensity enhancement, and thermal resistance loss distributions for the optimized size (core-shell size of 24 nm/12 nm)

and thermal resistance loss distributions for the optimized size and wavelength. An enhanced near electric field can be seen in the outer surface of the NP, and an enhanced thermal resistance loss can be obtained in the inner cavity of the NP. The maximum temperature increase  $\Delta T$  was obtained at different incident light intensities as shown in Fig. 7b. Due to the existence of TBCs, temperature differences were observed between the electrons and the lattice, the electrons and the dielectric, and the NP and the surrounding water. All these barriers and high absorption ability led to a temperature increase in the NP region.

## Discussion

To further understand the optimized results in the local heating, photothermal conversion, absorption efficiency, and absorption cross section, a factor  $\psi(x)$  was defined as:

$$\psi(x) = \frac{\sigma_{\text{abs}}}{R^x} \quad (17)$$

where  $\sigma_{\text{abs}}$  is the absorption cross section.  $R$  is the NP radius and  $x$  is the variable. It can be seen that for the optimization of absorption cross section, the target is  $\psi(0)$  (i.e.,  $\sigma_{\text{abs}}$ ). For the optimization of local heating, we can see from the maximum temperature of the surrounding medium in the interface of the NP and the surrounding environment, which can be obtained as:

$$\Delta T_w = \frac{\sigma_{\text{abs}} I_{\text{in}}}{4\pi R k_w} \sim \frac{\sigma_{\text{abs}}}{R} = \psi(1) \quad (18)$$

Similarly, the optimized target for the photothermal conversion ability and absorption efficiency can be obtained as  $\psi(3)$  and  $\psi(2)$  respectively. Figure 8 shows the comparison between different optimized targets with a normalized processing function  $\psi(x)$ . It can be seen that

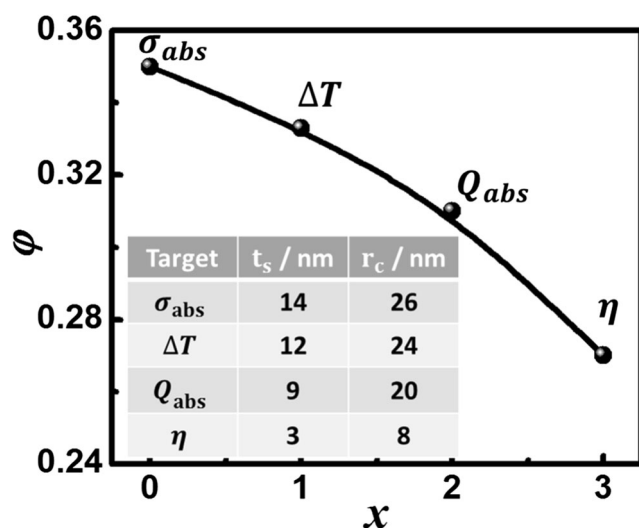


Fig. 8 Optimized core-shell ratios and core-shell sizes with different targets at 600 nm

the optimized core-shell ratio decreased with increasing the value of  $x$ . And both the optimized core sizes and shell sizes decreased with increasing the value of  $x$ . On the other hand, based the discussed above, we can see that all optimized core-shell NPs obtained the LSPR at  $\sim 600$  nm for different targets. It indicated that in the optimization process, not only do we need to find the LSPR wavelength at the optimized wavelengths but also the size parameters need to be further optimized for different applications. Based on our results, it can be obtained that a smaller optimized core-shell size was obtained with a consideration of greater effect of the NP radius (i.e., larger value of  $x$  in Eq. 18). Finally, for the practical applications, it can be seen from Figs. 4a, 5, 6, and 7a that the size parameters nearby the optimized results still have a relatively great performance. Therefore, it still has a great guidance for the design of the core-shell particles in the practical applications with a bit size errors.

## Conclusions

In conclusion, the near electric field enhancement, photothermal conversion, and local heating of Au@SiO<sub>2</sub> core-shell NPs were investigated numerically. For the near electric field enhancement, the optimal core-shell dimensions among the simulated SiO<sub>2</sub>@Au NP were 14 nm/6 nm, with maximum enhanced near electric field factors of 182. The optimized core-shell ratio decreased with increasing the optimized wavelength and the maximum intensity of near field increased rapidly and then changed slightly with increasing the optimized wavelengths since a gradually smaller core-shell ratio limited the LSPR intensity.

To obtain the maximum effective light absorption or photothermal conversion, the optimized core-shell dimensions were 8 nm/3 nm with an optimized photothermal conversion factor of 54. In the local heating or temperature increase, due to the existence of TBCs, a temperature drop is observed between the electrons and the lattice, the electrons and the dielectrics, and the NP and the surrounding water. All these barriers and high absorption ability lead to a temperature increase in the NP region. The optimal core-shell dimensions to maximize the local heating of the SiO<sub>2</sub>@Au NPs were 24 nm/12 nm at a wavelength of 600 nm.

Finally, the comparison between different optimized targets with a normalized processing function  $\psi(x)$  indicated optimized core-shell ratio and core-shell sizes decreased with increasing the value of  $x$ . All optimized core-shell NPs obtained the LSPR at  $\sim 600$  nm for different targets. But a smaller optimized core-shell size was obtained with a consideration of greater effect of the NP radius (i.e., larger value of  $x$  in Eq. 18).



**Funding information** This work was financially supported by the National Natural Science Foundation of China (Grant No. 51676060), the Natural Science Funds of Heilongjiang Province for Distinguished Young Scholars (Grant No. JC2016009), and the Science Creative Foundation for Distinguished Young Scholars in Harbin (Grant No. 2014RFYXJ004).

## References

- Shankar SS, Rizzello L, Cingolani R, Rinaldi R, Pompa PP (2009) Micro / nanoscale patterning of plasmonic applications. *Nano* 3: 893–900. <https://doi.org/10.1021/nn900077s>
- Takeda Y, Plaksin OA, Wang H, Kono K, Umeda N, Kishimoto N (2006) Surface plasmon resonance of au nanoparticles fabricated by negative ion implantation and grid structure toward plasmonic applications. *Opt Rev* 13:231–234. <https://doi.org/10.1007/s10043-006-0231-2>
- Ershov AE, Gavriluk AP, Karpov SV (2016) Plasmonic nanoparticle aggregates in high-intensity laser fields: effect of pulse duration. *Plasmonics* 11:403–410. <https://doi.org/10.1007/s11468-015-0054-8>
- Rycenga M, Cobley CM, Zeng J, Li W, Moran CH, Zhang Q, Qin D, Xia Y (2011) Controlling the synthesis and assembly of silver nanostructures for plasmonic applications. *Chem Rev* 111:3669–3712. <https://doi.org/10.1021/cr100275d>
- Catchpole KR, Polman A (2008) Plasmonic solar cells. *Opt Express* 16:21793. <https://doi.org/10.1364/OE.16.021793>
- Atwater HA, Polman A (2010) Plasmonics for improved photovoltaic devices. *Nat Mater* 9:205–213. <https://doi.org/10.1038/nmat2629>
- Brown MD, Suteewong T, Kumar RSS, D’Innocenzo V, Petrozza A, Lee MM, Wiesner U, Snaith HJ (2011) Plasmonic dye-sensitized solar cells using core-shell metal-insulator nanoparticles. *Nano Lett* 11:438–445. <https://doi.org/10.1021/nl1031106>
- Chueh C-C, Li C-Z, Jen AK-Y (2015) Recent progress and perspective in solution-processed interfacial materials for efficient and stable polymer and organometal perovskite solar cells. *Energy Environ Sci* 8:1160–1189. <https://doi.org/10.1039/C4EE03824J>
- Reineck P, Lee GP, Brick D, Karg M, Mulvaney P, Bach U (2012) A solid-state plasmonic solar cell via metal nanoparticle self-assembly. *Adv Mater* 24:4750–4755. <https://doi.org/10.1002/adma.201200994>
- Chen M, He Y, Zhu J, Kim DR (2016) Enhancement of photo-thermal conversion using gold nanofluids with different particle sizes. *Energy Convers Manag* 112:21–30. <https://doi.org/10.1016/j.enconman.2016.01.009>
- Chen M, He Y, Zhu J, Shuai Y, Jiang B, Huang Y (2015) An experimental investigation on sunlight absorption characteristics of silver nanofluids. *Sol Energy* 115:85–94. <https://doi.org/10.1016/j.solener.2015.01.031>
- Chen M, He Y, Liu X, Zhu J, Liu R (2017) Synthesis and optical properties of size-controlled gold nanoparticles. *Powder Technol* 311:25–33. <https://doi.org/10.1016/j.powtec.2017.01.087>
- Chen M, He Y, Huang J, Zhu J (2017) Investigation into Au nanofluids for solar photothermal conversion. *Int J Heat Mass Transf* 108:1894–1900. <https://doi.org/10.1016/j.ijheatmasstransfer.2017.01.005>
- Luo YL, Shiao YS, Huang YF (2011) Release of photoactivatable drugs from plasmonic nanoparticles for targeted cancer therapy. *ACS Nano* 5:7796–7804. <https://doi.org/10.1021/nn201592s>
- Huang X, Jain PK, El-Sayed IH, El-Sayed MA (2008) Plasmonic photothermal therapy (PPTT) using gold nanoparticles. *Lasers Med Sci* 23:217–228. <https://doi.org/10.1007/s10103-007-0470-x>
- He Y, Chen M, Wang X, Hu Y (2018) Plasmonic multi-thorny gold nanostructures for enhanced solar thermal conversion. *Sol Energy* 171:73–82. <https://doi.org/10.1016/j.solener.2018.06.071>
- Rahman IA, Padavettan V (2012) Synthesis of silica nanoparticles by sol-gel: size-dependent properties, surface modification, and applications in silica-polymer nanocomposites—a review. *J Nanomater* 2012:1–15. <https://doi.org/10.1155/2012/132424>
- Rao KS, El-Hami K, Kodaki T et al (2005) A novel method for synthesis of silica nanoparticles. *J Colloid Interface Sci* 289:125–131. <https://doi.org/10.1016/j.jcis.2005.02.019>
- Zhao J, Pinchuk AO, McMahon JM et al (2008) Methods for describing the electromagnetic properties of silver and gold nanoparticles. *Chem Soc Rev* 41:1710–1720
- Lu Y, Yin Y, Li ZY, Xia Y (2002) Synthesis and self-assembly of Au@SiO<sub>2</sub> core-shell colloids. *Nano Lett* 2:785–788. <https://doi.org/10.1021/nl025598i>
- Link S, Burda C, Nikoobakht B, El-Sayed MA (2000) Laser-induced shape changes of colloidal gold nanorods using femtosecond and nanosecond laser pulses. *J Phys Chem B* 104:6152–6163. <https://doi.org/10.1021/jp000679t>
- Qin Z, Bischof JC (2012) Thermophysical and biological responses of gold nanoparticle laser heating. *Chem Soc Rev* 41:1191–1217. <https://doi.org/10.1039/C1CS15184C>
- Meng L, Yu R, Qiu M, García De Abajo FJ (2017) Plasmonic nano-oven by concatenation of multishell photothermal enhancement. *ACS Nano* 11:7915–7924. <https://doi.org/10.1021/acsnano.7b02426>
- Lin Z, Zhigilei LV, Celli V (2008) Electron-phonon coupling and electron heat capacity of metals under conditions of strong electron-phonon nonequilibrium. *Phys Rev B - Condens Matter Mater Phys* 77:1–17. <https://doi.org/10.1103/PhysRevB.77.075133>
- Plech A, Kotaidis V, Grésillon S, Dahmen C, von Plessen G (2004) Laser-induced heating and melting of gold nanoparticles studied by time-resolved x-ray scattering. *Phys Rev B - Condens Matter Mater Phys* 70:1–7. <https://doi.org/10.1103/PhysRevB.70.195423>
- Baffou G, Quidant R, García De Abajo FJ (2010) Nanoscale control of optical heating in complex plasmonic systems. *ACS Nano* 4: 709–716. <https://doi.org/10.1021/nn901144d>
- Lombard J, Detcheverry F, Merabia S (2015) Influence of the electron-phonon interfacial conductance on the thermal transport at metal/dielectric interfaces. *J Phys Condens Matter* 27:015007. <https://doi.org/10.1088/0953-8984/27/1/015007>
- Lalisse A, Tessier G, Plain J, Baffou G (2015) Quantifying the efficiency of plasmonic materials for near-field enhancement and photothermal conversion. *J Phys Chem C* 119:25518–25528. <https://doi.org/10.1021/acs.jpcc.5b09294>
- Chen M, He Y, Wang X, Hu Y (2018) Complementary enhanced solar thermal conversion performance of core-shell nanoparticles. *Appl Energy* 211:735–742. <https://doi.org/10.1016/j.apenergy.2017.11.087>